Plasmonic Nanoclusters with Rotational Symmetry: Polarization-Invariant Far-Field Response *vs* Changing Near-Field Distribution

Mohsen Rahmani,[†,⊥] Edward Yoxall,[†,⊥] Ben Hopkins,[‡,⊥] Yannick Sonnefraud,[†,*] Yuri Kivshar,[‡] Minghui Hong,[§] Chris Phillips,[†] Stefan A. Maier,[†] and Andrey E. Miroshnichenko[‡,*]

[†]Department of Physics, Imperial College London, London SW7 2AZ, U.K., [‡]Nonlinear Physics Centre, Research School of Physics and Engineering, Australian National University, Canberra, ACT 0200, Australia, and [§]Department of Electrical and Computer Engineering, National University of Singapore, 4 Engineering Drive 3, Singapore 117576. [⊥]M. Rahmani, E. Yoxall, and B. Hopkins contributed equally to this work.

ABSTRACT

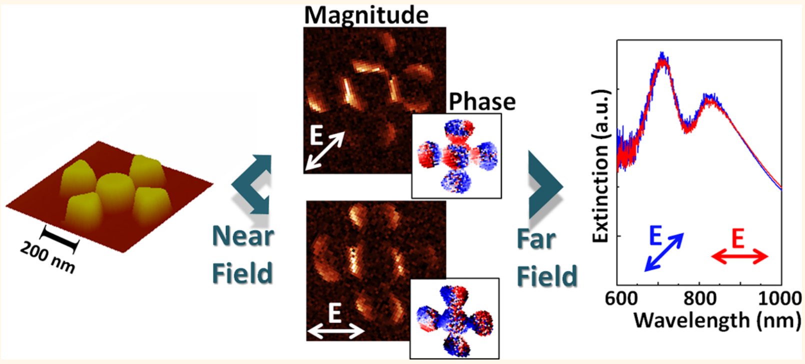

Flexible control over the near- and far-field properties of plasmonic nanostructures is important for many potential applications, such as surface-enhanced Raman scattering and biosensing. Generally, any change in the polarization of the incident light leads to a change in the nanoparticle's near-field distribution and, consequently, in its far-field properties as well. Therefore, producing polarization-invariant optical responses in the far field from a changing near field remains a challenging issue. In this paper, we probe experimentally the optical properties of cruciform pentamer structures—as an example of plasmonic oligomers—and demonstrate that they exhibit such behavior due to their symmetric geometrical arrangement. We demonstrate direct control over hot spot positions in sub-20 nm gaps, between disks of 145 nm diameter at a wavelength of 850 nm, by means of scattering scanning near-field optical microscopy. In addition, we employ the coupled dipole approximation method to define a qualitative model revealing the relationship between the near and far field in such structures. The near-field profiles depend on particular mode superpositions excited by the incident field and, thus, are expected to vary with the polarization. Consequently, we prove analytically that the far-field optical properties of pentamers have to be polarization-independent due to their rotational symmetry.

KEYWORDS: near-field optical microscopy · symmetry · polarization independence · plasmonic oligomers

Surface plasmons are currently a subject of intense interest due to their wide range of applications in both biological and physical sciences.[1] Localized surface plasmon resonances (LSPRs) in nanoparticles can create areas of high electromagnetic (EM) field enhancement, known as hot spots, on which many applications of plasmonics are based.[2−4] For instance, these field enhancements amplify Raman scattering, leading to what is known as surface-enhanced Raman scattering (SERS)[5] or surface-enhanced infrared absorption (SEIRA).[6,7] They can also transfer electromagnetic energy efficiently from the near to the far field. The effect of this can be seen in far-field absorption, scattering, and extinction cross section spectra.[1,4]

In complex structures, consisting of several nanoparticles, the EM coupling between

* Address correspondence to y.sonnefraud@imperial.ac.uk; andrey.miroshnichenko@anu.edu.au.

Received for review September 17, 2013 and accepted November 4, 2013.

Published online November 04, 2013
10.1021/nn404869c

the plasmon resonances of the individual elements results in hybridized plasmon modes.[8−11] These hybridized modes can display a wide range of interesting far-field properties, such as subradiance, superradiance, or asymmetric line shapes.[8−13] Their optical properties are highly sensitive to perturbations such as symmetry breaking, shape imperfections, and change of dielectric environment, which makes them well suited for sensing applications.[1−4] Dolmens, ring-disk cavities, and core−shell structures are examples exhibiting extraordinary near-field and far-field responses.[3,14−16] A common feature in such structures is that their optical responses are polarization-dependent. In other words, the strong variation of near-field intensity with the polarization of incident light has a direct influence on the far-field response of these structures. On the other hand, the design of structures for which the positions of near-field hot spots can be controlled by polarization (while maintaining an equal excitation efficiency, *i.e.*, equal extinction cross section) has received much less attention.

Recently, a number of research groups have reported the design of novel nanostructures with polarization-invariant far-field responses, such as metal−insulator−metal stacks with a nanostructured top silver film[17] and rotor-shaped structures.[18] Furthermore, some theoretical articles have predicted this effect in coupled dielectric waveguides[19] and petal nanoflowers.[20] In addition, theoretical studies have revealed a direct link between the polarization independence of all far-field cross sections and the nanostructures' rotational symmetry.[21] Planar symmetric clusters of plasmonic nanoparticles, also called oligomers,[5,10,22−31] have recently been proposed as candidates for polarization-independent far-field optical properties, while their near-field distribution varies.[21,32,33]

A number of studies have imaged the near-field patterns within oligomers using a variety of techniques,[34,5] including scattering-type scanning near-field optical microscopy (s-SNOM) in the mid infrared.[25,35,36] However, to date, a comprehensive study including experimental data showing the relationship between the near- and far-field properties of plasmonic nanoparticles with respect to the polarization is still missing. In this paper, we conduct such a study on planar pentamers in the near infrared as an example of a plasmonic oligomer.

In particular, here we show experimentally that the extinction spectra for different polarizations are identical. We develop an analytical model based on the coupled dipole approximation (CDA). This model allows us to analyze the optical response of the pentamer in terms of eigenmodes. It turns out that such a mode decomposition does depend on the incident polarization and so does the near-field distribution. At the same time, we rigorously prove that the far-field response is polarization-independent solely due to the geometric symmetry, without any additional conditions imposed on a given system, such as near-field distributions. Subsequently, we image the near-field distribution around the pentamer structure with an s-SNOM in the near-infrared (at 850 nm) to detect the hot spots in ~15 nm gaps between the pentamer disks, which are ~145 nm in diameter. Our near-field images are in very good agreement with theoretical predictions, showing clearly that the near-field distribution is highly polarization-dependent.

RESULTS AND DISCUSSION

Figure 1a demonstrates the scanning electron microscopy (SEM) image of Au pentamer arrays consisting of central circular disks surrounded by four triangle-shaped nanoparticles. The AFM image in the bottom left inset of Figure 1a shows that the particles' side walls are very close to vertical. The external diameters of all elements and interparticle gaps are 145 and 15 nm, respectively. The numerically simulated and experimentally measured optical responses of the pentamers for polarizations of 0, 45, and 90 degrees with respect to the *x*-axis are displayed in Figure 1b and c, respectively. Both numerical and experimental results show clearly that the far-field optical properties are independent of the polarization.

This invariance of the extinction cross sections with polarization can be explained by the geometrical symmetry of the pentamer nanoclusters. Indeed, it has recently been shown theoretically that the effect of polarization on the extinction, absorption, and scattering cross sections is inherently connected to the symmetry of the scattering system.[21] For any scattering system described through the CDA, the far-field cross sections σ can be expressed as the expectation value of the corresponding matrix $\hat{M}$ with the incident field polarization $\mathbf{E_0}$,

$$\sigma_i = \mathbf{E}_0^t \hat{M}_i \mathbf{E}_0 \qquad (1)$$

where i stands for extinction, scattering, or absorption cross section. Subsequently, by choosing to describe each cross section in terms of its related matrix $\hat{M}_i$, we are able to retain information on how the incident field's polarization affects the cross section for a given propagation direction. This form is useful for the analysis because it has been shown[21] that each matrix $\hat{M}$ must commute with the symmetry operators that correspond to the structure's symmetry. As such, we can relate the far-field cross sections to the structure's symmetry using well-established group-theory principles to constrain the shape of each $\hat{M}$ matrix based on the symmetry group of the associated system's geometry. In our case, the geometry of the pentamer oligomer will be invariant under the tetragonal group of symmetry operations (C_{4v}), where the operations are centered on the normal axis of the structure. Furthermore, as we only consider normal incidence for the pentamer system, we can neglect the *z*-direction and regard both the $\hat{M}$ matrix and C_{4v} symmetry operations as being two-dimensional. The two-dimensional symmetry

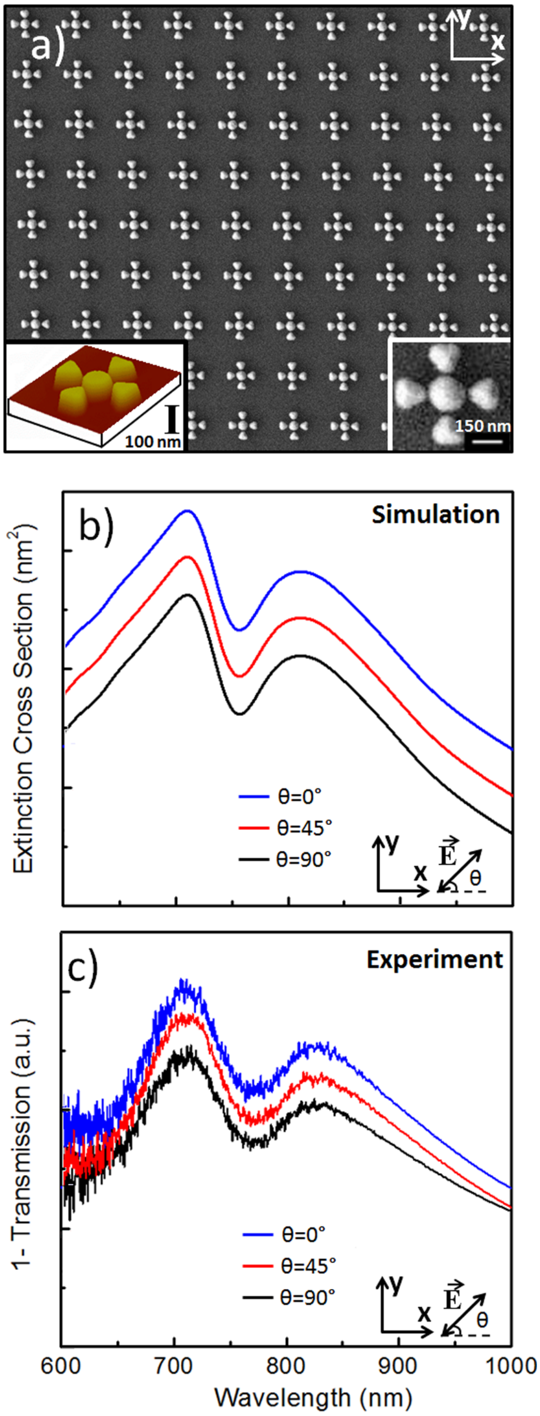

Figure 1. (a) SEM images of a periodic array of pentamers. The left inset shows an AFM image. The right inset is a close-up image of one pentamer. (b) Simulated extinction cross sections and (c) experimental extinction (1 − Transmission) spectra at polarization directions of 0°, 45°, and 90° with respect to the *x*-axis. Spectra for 45° and 90° are slightly shifted vertically to avoid their overlap.

operations for the pentamer are then from the doubly degenerate E irreducible representation of the C_{4v} symmetry group (see Table 1).

The direct application of Schur's Lemma requires that the only way the operator $\hat{M}$ can commute with all elements of this two-dimensional irreducible

TABLE 1. Character Table for the *E* Irreducible Representation of the C_{4v} Symmetry Group[a]

	C_{4v}		E	C_2	$2C_4$	$2\sigma_v$	$2\sigma_d$
(xz, yz)	$\left.\begin{matrix}(x, y)\\(R_x, R_y)\end{matrix}\right\}$	E	2	−2	0	0	0

[a] The matrix representation of any symmetry operation that acts on either the incident field or pentamer geometry will have the characters listed here.

representation without being trivial (*i.e.*, all zeros) is if $\hat{M}$ is a multiple of the identity matrix:

$$\hat{M}_i = \begin{pmatrix} a_i & 0 \\ 0 & a_i \end{pmatrix} \quad (a_i \in \mathscr{R}) \tag{2}$$

As such, all three cross sections of the pentamer at normal incidence must be proportional to the magnitude of the incident field only and are subsequently completely independent of polarization. Additionally, given that the optical theorem[37] directly relates the amplitude of the forward scattering to the extinction cross section, a corollary of what we have shown here is that the transmission of the pentamer will also be independent of polarization. Therefore, this gives the unintuitive prediction that the polarization-dependent near field does not affect these measures of scattering that exist in both the near and far fields.

To consider the near-field origin of such behavior in the pentamer structure, we analyze its response in terms of eigenmodes as described in ref 38. It is known that Fano resonances can be generated purely from the interference of nonorthogonal collective eigenmodes, which themselves can be identified based on the coupled-dipole approximation. As the size of the particles in the pentamer system is smaller than the wavelength, the dipole responses of the individual particles are dominant, and we can subsequently analyze the system's optical response qualitatively with an array of coupled dipoles. In Figure 2, the CDA applied to the pentamer system with spherical particles (whereas the experiment uses four triangular particles around a central disk) shows a qualitative correlation with the experimental results and, thus, justifies this approach. It is worth noting that, as long as the dipole polarization is a concern, the difference in the shape results only in a change of the constants in the polarizability expression and the dependence of the polarizability on the problem's parameters essentially remains the same. Thus a particle absorbs or emits radiation as a point-like dipole. This justifies that Au nanospheres can be used in analytical calculations (based on the Mie scattering method) to predict the optical responses of Au nanodisks.[13,23]

The effect of symmetry can be investigated analytically, without explicitly solving for the pentamer's eigenmodes, because each eigenmode must be either

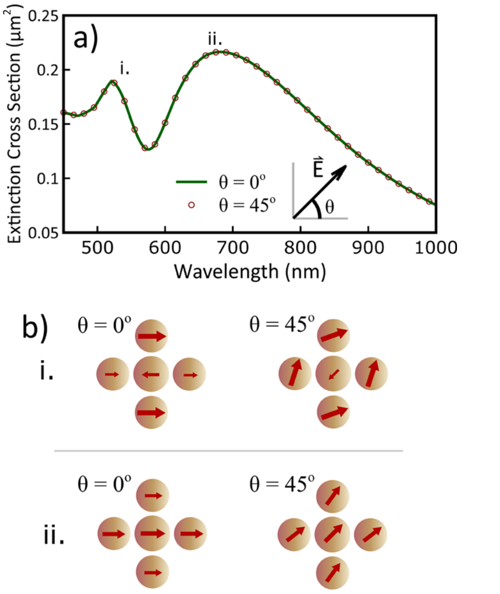

Figure 2. CDA simulation results of a gold nanosphere pentamer under two different polarizations showing (a) extinction spectra and (b) associated near-field dipole moment profiles at the two extinction peaks i and ii. The extinction spectra show a qualitative match to that of the experiment and a complete independence of the incident light's polarization despite near-field variations. The pentamer system here is constructed of nanospheres in free space, where the central nanosphere has a 145 nm diameter and the outer nanospheres have 135 nm diameters with 15 nm interparticle separations. Dipole profiles show only the real components of the dipole moments, which are defined as being in phase with the incident field.

degenerate with or identical to their own symmetry-operated version, which is also itself an eigenmode. In order to consider the eigenmodes rigorously, the pentamer's response will be described by the dipole moment vectors at each of the five particles. To denote and emphasize this point, we will express both the pentamer's response and the field acting on it as the concatenation of all the dipole moment vectors or the incident field vectors at each particle (respectively). We will use state "bra-ket" notation to differentiate these new concatenated vectors from their constituent three-element vectors. In this sense, the symmetry operations, which act on these concatenated vector states, will be described by unitary matrices. To begin, we consider some basis of linearly independent eigenmodes of the pentamer system $\{|\upsilon_i\rangle\}$, which span the space of all possible incident field polarizations. In such a basis, each incident field state will have a unique decomposition into the pentamer's eigenmodes. So we can express an x-polarized incident field $|E_x\rangle$ and the corresponding response of the system $|F(\mathbf{E}_x)\rangle$ as a linear combination of eigenmodes:

$$|E_x\rangle = \sum_i a_i|\upsilon_i\rangle \Rightarrow |F(\mathbf{E_x})\rangle = \sum_i a_i\lambda_i|\upsilon_i\rangle \quad (a_i, \lambda_i \in C) \quad (3)$$

where λ_i is the eigenvalue of $|\upsilon_i\rangle$ and the set of a_i are the unique coefficients in the linear combination of eigenvectors that describes the x-polarized incident field.

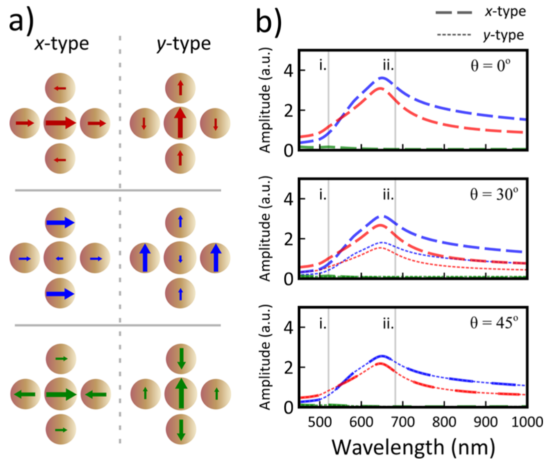

Figure 3. Simulation results showing (a) profiles of the six eigenmodes that describe all the responses of the pentamer structure under normal-incidence plane-wave excitation and (b) the corresponding eigenmode decomposition of the pentamer's response at three different polarizations. Degeneracy between the *x*- and *y*-polarized eigenmodes is labeled as being *x*- and *y*-type. All eigenmode profiles are for the wavelength denoted with ii and, thus, show only the real components of the dipole moments, defined as being in-phase with the incident field.

We can then relate x- and y-polarized incident fields through the rotation of the whole system by $\pi/2$, and, given that this rotation is a symmetry operation $\hat{R}$, the rotated eigenmodes $\hat{R}|\upsilon_i\rangle$ will still be eigenmodes of the system. Therefore a y-polarized incident field can be written in terms of the eigenmode decomposition of the x-polarized incident field as

$$|E_y\rangle = \hat{R}|E_x\rangle = \sum_i a_i\hat{R}|\upsilon_i\rangle \quad (4)$$

For the pentamer system, therefore, a corollary of the degeneracy of its eigenmodes under symmetry operations is that any eigenmode excited by an x-polarized field will have a degenerate partner that is excited by a y-polarized field. This is in agreement with the irreducibility postulate,[39,40] which states that any eigenmode associated with a doubly degenerate irreducible representation must itself be 2-fold degenerate. This degeneracy can be observed in Figure 3. Moreover, this figure shows that the response of the system at multiple polarizations can be expressed in terms of no more than six distinct eigenmodes.

We can then take advantage of the fact that any weighted sum of the x and y eigenmodes in a degenerate pair must itself be an eigenmode and share the same eigenvalue as both the original eigenmodes.

$$|\upsilon_i'\rangle = x|\upsilon_i\rangle + y\hat{R}|\upsilon_i\rangle \quad (x, y \in C) \quad (5)$$

The decomposition of an arbitrarily polarized incident field into the x and y components will always result in a weighted sum of the degenerate x-type and y-type eigenmodes. Each eigenmode pair can therefore be presented in terms of a single eigenmode that will be degenerate with any other weighted sum of the same x and y eigenmodes (*i.e.*, other polarizations).

$$\begin{aligned} |E_0\rangle &= x|E_x\rangle + y|E_y\rangle \\ &= x(\sum_i a_i|\upsilon_i\rangle) + y(\sum_i a_i\hat{R}|\upsilon_i\rangle) \\ &= \sum_i a_i|\upsilon_i'\rangle \end{aligned} \tag{6}$$

This is then the origin of polarization invariance in the pentamer structure; the eigenmodes excited by

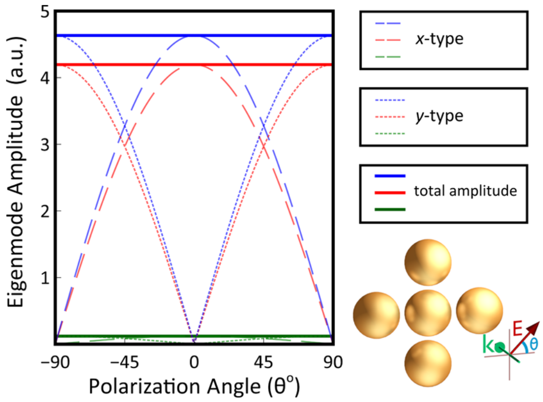

Figure 4. Dependence of each eigenmode's amplitude ($a_i\lambda_i$) with polarization. Importantly this shows that the total amplitude of an eigenmode, *i.e.*, the magnitude of the combined *x*- and *y*-type eigenmodes, is independent of polarization angle. The wavelength used in this figure is that denoted by ii in both Figures 2 and 3

one polarization will be degenerate with those excited by any other polarization. However, for completeness, we must also show that the x and y eigenmodes of each degenerate pair are orthogonal, otherwise the magnitude of each vector υ'_i is not necessarily conserved as the polarization varies. This is best done by taking advantage of the effect the reflection operations $\hat{\sigma}$ in C_{4v} have on the incident field polarization. If we consider the reflection with respect to the x-axis we obtain

$$\hat{\sigma}_x|E_x\rangle = |E_x\rangle, \quad \hat{\sigma}_x|E_y\rangle = -|E_y\rangle \tag{7}$$

However, as there is only one unique linear combination of each incident field ($|E_x\rangle$, $|E_y\rangle$) in terms of the linearly independent eigenmodes (see eq 3), the only possible transformation of each $|\upsilon_i\rangle$ and associated $\hat{R}|\upsilon_i\rangle$ (where $a_i \neq 0$) under this reflection operation is

$$\hat{\sigma}_x|\upsilon_i\rangle = |\upsilon_i\rangle, \quad \hat{\sigma}_x\hat{R}|\upsilon_i\rangle = -\hat{R}|\upsilon_i\rangle \tag{8}$$

This statement then requires that such eigenmodes of a degenerate pair ($|\upsilon_i\rangle$ and $\hat{R}|\upsilon_i\rangle$) are orthogonal as follows:

$$\begin{aligned} \langle\upsilon_i|\hat{R}|\upsilon_i\rangle &= \langle\upsilon_i|(\hat{\sigma}_x^t\hat{\sigma}_x)\hat{R}|\upsilon_i\rangle = (\langle\upsilon_i|\hat{\sigma}_x^t)(\hat{\sigma}_x\hat{R}|\upsilon_i\rangle) \\ &= -\langle\upsilon_i|\hat{R}|\upsilon_i\rangle \Longrightarrow \langle\upsilon_i|\hat{R}|\upsilon_i\rangle = 0 \end{aligned} \tag{9}$$

Therefore, the polarization of the incident field cannot affect either the decomposition of the field into nondegenerate eigenmodes $|\upsilon'_i\rangle$ or their amplitudes a_i.

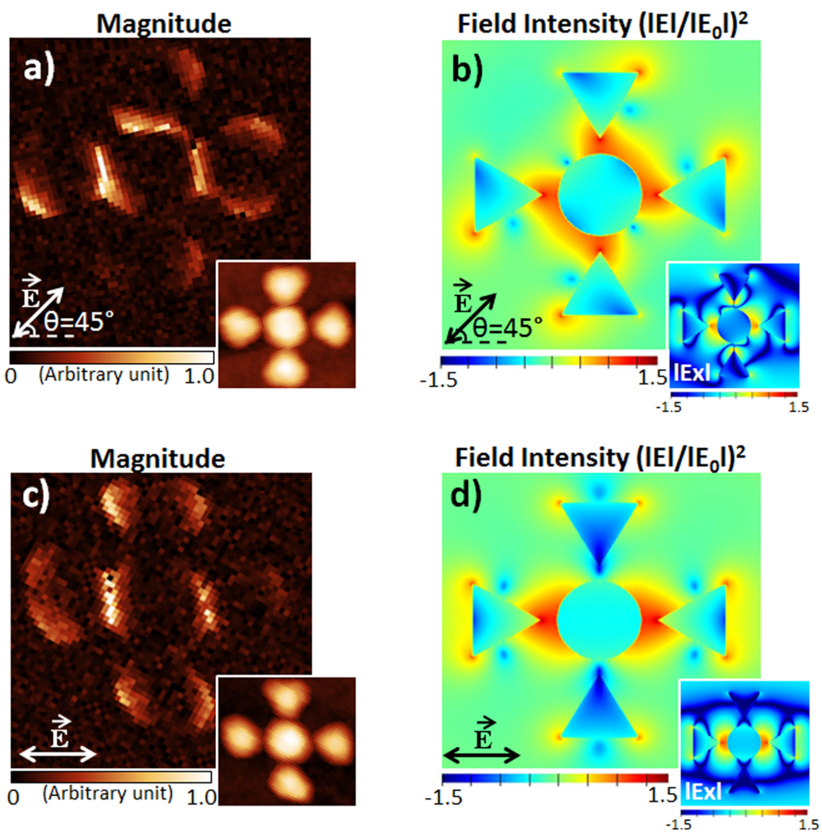

Figure 5. (a, c) Measured near-field scattering magnitude. (b, d) Simulated field intensity ($(|E|/|E_0|)^2$) (logarithmic scale) for incident polarizations of 45° and 0°, compared to the *x*-axis, respectively. Insets in (a) and (c) show the AFM topography of the pentamer, and those in (b) and (d) display the in-plane *x* component of the electric field.

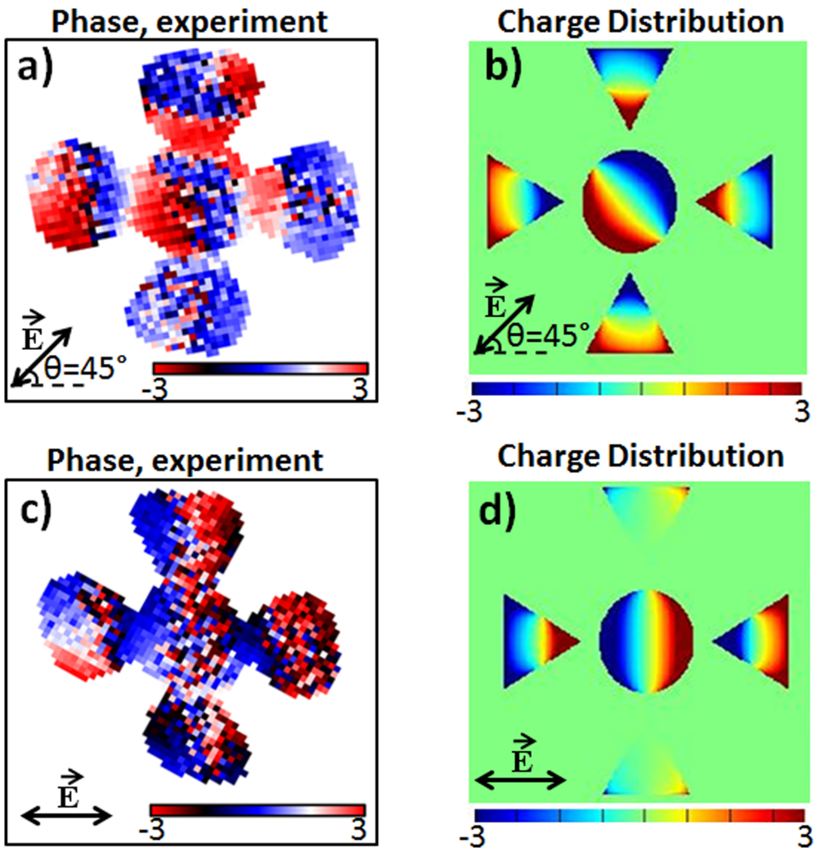

Figure 6. (a, c) Measured near-field scattering phase. (b, d) Simulated charge distributions at incident polarization direction along 45° and 0°, respectively.

This result can be seen in Figure 4, where the amplitude of each nondegenerate eigenmode remains constant with polarization, in spite of the fact that the projections onto the constituent *x*- and *y*-type eigenmodes are varying. In this sense the polarization of the incident field can be considered as only controlling the "polarization" of the eigenmodes it induces, that is, the *x* and *y* projections that create $|\upsilon'_i\rangle$. It is worth noting that a dynamic coupled dipole approximation, using different formalisms, can also be utilized to reach similar conclusions.[41]

To complete this analysis, we show that, although the far-field cross sections of the pentamers are polarization-invariant, the near-field distribution depends strongly on the incident polarization. Figure 5 compares the measured near-field scattering magnitude with the simulated near-field intensity $(|\mathbf{E}|/|\mathbf{E_0}|)^2$ at $\lambda = 850$ nm for different polarizations. This is close to the wavelength of the second extinction peak (see Figure 1) at which the near-field intensity is at its highest.[42−44] It is worth noting that although some theoretical studies have modeled the near-field distribution in oligomers in the visible and near-IR range, direct experimental measurements at this frequency range have not been reported so far.

The images are taken with s-polarized illumination. As this polarization is only weakly concentrated by the s-SNOM probe, the scattered signal it produces is only weakly affected by the "chemical" differences between the glass and the gold[45] and is dominantly due to the field of the plasmon resonance. Typically, measurements of this type are done with a "cross-polarization" scheme, *i.e.*, s-polarized illumination and p-polarized detection, so as to be sensitive to the vertical component of the plasmon's field distribution.[25,46−48] However, for this particular structure, this has the unfortunate effect of masking the "hot spots" (where the plasmon fields are largely horizontal); so here we detect the images in the s-polarization as well. For further details of the setup employed, see Figure S3 in the Supporting Information. The rotation of the polarization in the experiments is achieved by rotating the sample, keeping all the parameters unchanged.

As can be seen in Figure 5, the numerical and experimental results are in a good agreement with only slight discrepancies. These arise mostly from retardation effects, caused by the fact that the illuminating beam is not impinging at normal incidence, but 60° off it due to experimental limitations (see Figures S2 and S3 in the Supporting Information), although slight imperfections in the fabrication process (leading to variations in shape or refractive index across the structure) may also play a role. The phase of the illuminating field is therefore not constant across the sample, as it is assumed to be in the simulations.

Figure 6 shows the phase of the measured near-field scattering signal at the same wavelength (850 nm) as Figure 5. The measured phase corresponds to the relative phase of the near-field resonances, the source of which being particular distributions of positive and negative charge. The phase should therefore mirror the charge distribution. Again, Figure 6 shows a good match between experiment and simulation. As can be seen in near-field optical properties shown in Figures 5 and 6, both magnitude and phase in the plasmonic pentamer are highly affected by the polarization direction.

CONCLUSIONS

We have studied the near- and far-field optical properties of pentamer nanostructures as an example of plasmonic oligomers. We have shown analytically that the polarization of the incident field cannot affect the decomposition of the field into nondegenerate eigenmodes or their projection onto the incident field. We have proven rigorously that the far-field polarization-independent response comes solely from the overall symmetry of the pentamer's geometry, and no extra conditions need to be imposed on the near-field distribution. We have observed experimentally that, in close agreement with our theory, the extinction cross section of the pentamers is independent of the polarization. Furthermore, the examination of the near-field distribution in the pentamers using an s-SNOM showed that the distribution is strongly dependent on the polarization of the incident light. The pentamer structures, therefore, offer the ability to move hot spots into different 15 nm gaps by rotating the incident light polarization, without loss of the excitation efficiency for any configuration. This property, which should be a general property of plasmonic oligomers exhibiting rotational symmetry, is very promising for nanoscale control of hot spot position and sensing.

METHODS

The arrays of Au pentamers, consisting of central circular disks surrounded by triangular-shaped components on a quartz substrate, are fabricated by electron beam lithography (Elonix 100KV EBL system). Each array has a dimension of $50 \times 50\,\mu m^2$, and it consists of 60 nm thick Au nanoparticles. A 3 nm thick Ti film is deposited on the substrate by e-beam evaporation (EB03 BOC Edwards) to increase the adhesion between Au and quartz, followed by the evaporation of a 60 nm thick Au film and a spin-coated 50 nm thick layer of hydrogen silsesquioxane as a negative electroresist. After baking the sample at 200 °C for 2 min, a combined process of e-beam exposure, development, and ion-milling is performed to create well-defined Au oligomers on the substrate. The surface morphology of the fabricated structures is characterized by high-resolution scanning electron microscopy (SEM) and atomic force microscopy (AFM).

Spectroscopic characterization of the fabricated nanoparticle arrays is carried out with a Bruker Hyperion 2000 Fourier transform infrared microscope installed with a 36×, NA = 0.5 objective. The transmission (T) spectrum of each nanoparticle array is obtained by normalizing the transmittance curve from an array-encapsulated area with a reference spectrum taken from a bare area in close proximity to the array. Finally, the extinction spectrum for each array is defined as (1 − T). To map the near-field distribution around the pentamer structure, s-SNOM is used. This technique operates by focusing light onto the apex of a very sharp probe (radius typically >10 nm) that is oscillating close to the sample surface. The backscattered light from the probe is collected and combined with a reference beam in a heterodyne detection scheme. By processing this combined demodulated signal at frequencies corresponding to the higher harmonics of the probe oscillation (typically the third harmonic for near-infrared light), the magnitude and phase of the near-field component on the sample surface can be inferred, and its distribution can thus be mapped out by scanning the tip across the sample. The key reason for using this approach is its resolution; unlike diffraction-limited techniques, the resolution is determined by the radius of curvature of the tip of the probe, and it can be many times smaller than the wavelength of the illuminating light.

Three-dimensional simulations are employed to calculate the extinction cross sections of individual nanostructures by using a commercially available finite-difference-time-domain code (Lumerical FDTD). Lumerical FDTD is used to predict near-field and far-field properties of proposed pentamers with similar dimensions and with full consideration of the substrate effect, as can be seen in Figures 1, 5, and 6. The dipole models used for Figures 2, 3, and 4 are performed with three-dimensional coupled electric and magnetic dipole approximation, using electric and magnetic polarizabilities derived from the exact scattering coefficients of Mie theory. Eigenmodes are then calculated numerically from the interaction matrix of the coupled-dipole simulation. Gold permittivity data, used in all simulations and calculations, was taken from ref 49.

Conflict of Interest: The authors declare no competing financial interest.

Supporting Information Available: Additional numerical simulations of pentamer at non-normal incidence and detailed explanation of the experimental s-SNOM setup. This material is available free of charge *via* the Internet at http://pubs.acs.org.

Acknowledgment. The authors acknowledge funding provided by the EPSRC Active Plasmonics Programme as well as the Leverhulme Trust. A.E.M. acknowledges the financial support from the Australian Research Council, including the Future Fellowship program (FT110100037). Y.S. acknowledges funding from the European Science Foundation, grants 4370 and 5214. The authors gratefully acknowledge use of the facilities of Data Storage Institute, (A*STAR) Agency for Science, Technology and Research, Singapore for sample fabrication and SEM imaging.

REFERENCES AND NOTES

1. Maier, S. A. *Plasmonics: Fundamentals and Applications*; Springer: Berlin, 2007.
2. Halas, N. J.; Lal, S.; Chang, W.-S.; Link, S.; Nordlander, P. Plasmons in Strongly Coupled Metallic Nanostructures. *Chem. Rev.* **2011**, *111*, 3913.
3. Giannini, V.; Fernández-Domínguez, A. I.; Heck, S. C.; Maier, S. A. Plasmonic Nanoantennas: Fundamentals and Their Use in Controlling the Radiative Properties of Nanoemitters. *Chem. Rev.* **2011**, *111*, 3888.
4. Stockman, M. I. Nanoplasmonics: Past, Present, and Glimpse into Future. *Opt. Express* **2011**, *19*, 22029–22106.
5. Ye, J.; Wen, F.; Sobhani, H.; Lassiter, J. B.; Dorpe, P. V.; Nordlander, P.; Halas, N. J. Plasmonic Nanoclusters: Near

Field Properties of the Fano Resonance Interrogated with SERS. *Nano Lett.* **2012**, *12*, 1660–1667.
6. Lal, S.; Grady, N. K.; Kundu, J.; Levin, C. S.; Lassiter, J. B.; Halas, N. J. Tailoring Plasmonic Substrates for Surface Enhanced Spectroscopies. *Chem. Soc. Rev.* **2008**, *37*, 898–911.
7. Le, F.; Brandl, D. W.; Urzhumov, Y. A.; Wang, H.; Kundu, J.; Halas, N. J.; Aizpurua, J.; Nordlander, P. Metallic Nanoparticle Arrays: A Common Substrate for Both Surface-Enhanced Raman Scattering and Surface-Enhanced Infrared Absorption. *ACS Nano* **2008**, *2*, 707–718.
8. Luk'yanchuk, B.; Zheludev, N. I.; Maier, S. A.; Halas, N. J.; Nordlander, P.; Giessen, H.; Chong, C. T. The Fano Resonance in Plasmonic Nanostructures and Metamaterials. *Nat. Mater.* **2010**, *9*, 707–715.
9. Miroshnichenko, A. E.; Flach, S.; Kivshar, Y. S. Fano Resonances in Nanoscale Structures. *Rev. Mod. Phys.* **2010**, *82*, 2257.
10. Rahmani, M.; Luk'yanchuk, B.; Hong, M. Fano Resonance in Novel Plasmonic Nanostructures. *Laser Photonics Rev.* **2012**, *7*, 329–349.
11. Prodan, E.; Radloff, C.; Halas, N.; Nordlander, P. A Hybridization Model for the Plasmon Response of Complex Nanostructures. *Science* **2003**, *302*, 419–422.
12. Sonnefraud, Y.; Leen Koh, A.; McComb, D. W.; Maier, S. A. Nanoplasmonics: Engineering and Observation of Localized Plasmon Modes. *Laser Photonics Rev.* **2012**, *6*, 277–295.
13. Rahmani, M.; Miroshnichenko, A. E.; Lei, D. Y.; Luk'yanchuk, B.; Tribelsky, M. I.; Kuznetsov, A. I.; Kivshar, Y. S.; Francescato, Y.; Giannini, V.; Hong, M. Beyond the Hybridization Effects in Plasmonic Nanoclusters: Diffraction-Induced Enhanced Absorption and Scattering. *Small* **2013**, 10.1002/smll.201301419.
14. Sonnefraud, Y.; Verellen, N.; Sobhani, H.; Vandenbosch, G. A.; Moshchalkov, V. V.; Van Dorpe, P.; Nordlander, P.; Maier, S. A. Experimental Realization of Subradiant, Superradiant, and Fano Resonances in Ring/Disk Plasmonic Nanocavities. *ACS Nano* **2010**, *4*, 1664–1670.
15. Mukherjee, S.; Sobhani, H.; Lassiter, J. B.; Bardhan, R.; Nordlander, P.; Halas, N. J. Fanoshells: Nanoparticles with Built-in Fano Resonances. *Nano Lett.* **2010**, *10*, 2694–2701.
16. Verellen, N.; Sonnefraud, Y.; Sobhani, H.; Hao, F.; Moshchalkov, V. V.; Dorpe, P. V.; Nordlander, P.; Maier, S. A. Fano Resonances in Individual Coherent Plasmonic Nanocavities. *Nano Lett.* **2009**, *9*, 1663–1667.
17. Aydin, K.; Ferry, V. E.; Briggs, R. M.; Atwater, H. A. Broadband Polarization-Independent Resonant Light Absorption Using Ultrathin Plasmonic Super Absorbers. *Nat. Commun.* **2011**, *2*, 517.
18. Rahmani, M.; Lukiyanchuk, B.; Liew, T.; Hong, M. In *Planar Isotropic Rotor-Shaped Nanostructures: An Alternative to Develop Oligomers*; Lasers and Electro-Optics (CLEO), 2012 Conference; IEEE, **2012**; pp 1−2.
19. Liu, W.; Sukhorukov, A. A.; Miroshnichenko, A. E.; Poulton, C. G.; Xu, Z.; Neshev, D. N.; Kivshar, Y. S. Complete Spectral Gap in Coupled Dielectric Waveguides Embedded into Metal. *Appl. Phys. Lett.* **2010**, *97*, 021106–021106-3.
20. Giannini, V.; Rodríguez-Oliveros, R.; Sánchez-Gil, J. A. Surface Plasmon Resonances of Metallic Nanostars/Nanoflowers for Surface-Enhanced Raman Scattering. *Plasmonics* **2010**, *5*, 99–104.
21. Hopkins, B.; Liu, W.; Miroshnichenko, A.; Kivshar, Y. Optically-Isotropic Responses Induced by Discrete Rotational Symmetry of Nanoparticle Clusters. *Nanoscale* **2013**, *5*, 6395–6403.
22. Rahmani, M.; Lei, D. Y.; Giannini, V.; Lukiyanchuk, B.; Ranjbar, M.; Liew, T. Y. F.; Hong, M.; Maier, S. A. Subgroup Decomposition of Plasmonic Resonances in Hybrid Oligomers: Modeling the Resonance Lineshape. *Nano Lett.* **2012**, *12*, 2101–2106.
23. Hentschel, M.; Saliba, M.; Vogelgesang, R.; Giessen, H.; Alivisatos, A. P.; Liu, N. Transition from Isolated to Collective Modes in Plasmonic Oligomers. *Nano Lett.* **2010**, *10*, 2721–2726.
24. Fan, J. A.; Wu, C.; Bao, K.; Bao, J.; Bardhan, R.; Halas, N. J.; Manoharan, V. N.; Nordlander, P.; Shvets, G.; Capasso, F. Self-Assembled Plasmonic Nanoparticle Clusters. *Science* **2010**, *328*, 1135–1138.
25. Alonso-Gonzalez, P.; Schnell, M.; Sarriugarte, P.; Sobhani, H.; Wu, C.; Arju, N.; Khanikaev, A.; Golmar, F.; Albella, P.; Arzubiaga, L. Real-Space Mapping of Fano Interference in Plasmonic Metamolecules. *Nano Lett.* **2011**, *11*, 3922–3926.
26. Hentschel, M.; Dregely, D.; Vogelgesang, R.; Giessen, H.; Liu, N. Plasmonic Oligomers: The Role of Individual Particles in Collective Behavior. *ACS Nano* **2011**, *5*, 2042–2050.
27. Zhang, Y.; Wen, F.; Zhen, Y.-R.; Nordlander, P.; Halas, N. J. Coherent Fano Resonances in a Plasmonic Nanocluster Enhance Optical Four-Wave Mixing. *Proc. Natl. Acad. Sci. U.S.A.* **2013**, *110*, 9215–9219.
28. Lassiter, J. B.; Sobhani, H.; Fan, J. A.; Kundu, J.; Capasso, F.; Nordlander, P.; Halas, N. J. Fano Resonances in Plasmonic Nanoclusters: Geometrical and Chemical Tunability. *Nano Lett.* **2010**, *10*, 3184–3189.
29. Wen, F.; Ye, J.; Liu, N.; Van Dorpe, P.; Nordlander, P.; Halas, N. J. Plasmon Transmutation: Inducing New Modes in Nanoclusters by Adding Dielectric Nanoparticles. *Nano Lett.* **2012**, *12*, 5020–5026.
30. Chang, W.-S.; Lassiter, J. B.; Swanglap, P.; Sobhani, H.; Khatua, S.; Nordlander, P.; Halas, N. J.; Link, S. A Plasmonic Fano Switch. *Nano Lett.* **2012**, *12*, 4977–4982.
31. Yang, J.; Rahmani, M.; Teng, J.; Hong, M. Magnetic-Electric Interference in Metal-Dielectric-Metal Oligomers: Generation of Magneto-Electric Fano Resonance. *Opt. Mater. Express* **2012**, *2*, 1407–1415.
32. Bao, K.; Mirin, N. A.; Nordlander, P. Fano Resonances in Planar Silver Nanosphere Clusters. *Appl. Phys. A: Mater. Sci. Process.* **2010**, *100*, 333–339.
33. Sheikholeslami, S. N.; García-Etxarri, A.; Dionne, J. A. Controlling the Interplay of Electric and Magnetic Modes via Fano-like Plasmon Resonances. *Nano Lett.* **2011**, *11*, 3927–3934.
34. Jäger, S.; Kern, A. M.; Hentschel, M.; Jäger, R.; Braun, K.; Zhang, D.; Giessen, H.; Meixner, A. J. Au-Nanotip as Luminescent Near-Field Probe. *Nano Lett.* **2013**, *13*, 3566–3570.
35. Weber, D.; Albella, P.; Alonso-González, P.; Neubrech, F.; Gui, H.; Nagao, T.; Hillenbrand, R.; Aizpurua, J.; Pucci, A. Longitudinal and Transverse Coupling in Infrared Gold Nanoantenna Arrays: Long Range versus Short Range Interaction Regimes. *Opt. Express* **2011**, *19*, 15047–15061.
36. Alonso-González, P.; Albella, P.; Schnell, M.; Chen, J.; Huth, F.; García-Etxarri, A.; Casanova, F.; Golmar, F.; Arzubiaga, L.; Hueso, L. Resolving the Electromagnetic Mechanism of Surface-Enhanced Light Scattering at Single Hot Spots. *Nat. Commun.* **2012**, *3*, 684.
37. Van de Hulst, H. On the Attenuation of Plane Waves by Obstacles of Arbitrary Size and Form. *Physica* **1949**, *15*, 740–746.
38. Hopkins, B.; Poddubny, A. N.; Miroshnichenko, A.; Kivshar, Y. Revisiting the Physics of Fano Resonances in Nanoparticle Oligomers. *arXiv:1310.2983v1*, **2013**.
39. McWeeny, R. *Symmetry: an Introduction to Group Theory and its Applications*; Dover Publications, 2002.
40. McIsaac, P. Symmetry-Induced Modal Characteristics of Uniform Waveguides−I: Summary of Results. *IEEE Trans. Microwave Theory Tech.* **1975**, *23*, 421–429.
41. Wang, M.; Cao, M.; Guo, Z.; Gu, N. Two-Step Decomposition of Plasmon Coupling in Plasmonic Oligomers. *J. Phys. Chem. C* **2013**, *117*, 11713–11717.
42. Rahmani, M.; Lukiyanchuk, B.; Tahmasebi, T.; Lin, Y.; Liew, T.; Hong, M. Polarization-Controlled Spatial Localization of Near-Field Energy in Planar Symmetric Coupled Oligomers. *Appl. Phys. A: Mater. Sci. Process.* **2012**, *107*, 23–30.
43. Rahmani, M.; Lukiyanchuk, B.; Ng, A.; Tavakkoli, K. G.; Liew, Y. F.; Hong, M. H. Generation of Pronounced Fano Resonances and Tuning of Subwavelength Spatial Light Distribution in Plasmonic Pentamers. *Opt. Express* **2011**, *19*, 4949–4956.
44. Rahmani, M.; Tahmasebi, T.; Lin, Y.; Lukiyanchuk, B.; Liew, T.; Hong, M. Influence of Plasmon Destructive Interferences on Optical Properties of Gold Planar Quadrumers. *Nanotechnology* **2011**, *22*, 245204.

45. Keilmann, F.; Hillenbrand, R. Near-Field Microscopy by Elastic Light Scattering from a Tip. *Philos. Trans. R. Soc. London, Ser. A* **2004**, *362*, 787–806.
46. Jones, A. C.; Olmon, R. L.; Skrabalak, S. E.; Wiley, B. J.; Xia, Y. N.; Raschke, M. B. Mid-IR Plasmonics: Near-Field Imaging of Coherent Plasmon Modes of Silver Nanowires. *Nano Lett.* **2009**, *9*, 2553–2558.
47. Dorfmuller, J.; Vogelgesang, R.; Weitz, R. T.; Rockstuhl, C.; Etrich, C.; Pertsch, T.; Lederer, F.; Kern, K. Fabry-Pérot Resonances in One-Dimensional Plasmonic Nanostructures. *Nano Lett.* **2009**, *9*, 2372–2377.
48. Vogelgesang, R.; Dmitriev, A. Real-Space Imaging of Nanoplasmonic Resonances. *Analyst* **2010**, *135*, 1175–1181.
49. Johnson, P. B.; Christy, R. Optical Constants of the Noble Metals. *Phys. Rev. B* **1972**, *6*, 4370.